ADVANCED OPTICAL MATERIALS
www.advopticalmat.de

Reconfigurable Parfocal Zoom Metalens

Fan Yang, Hung-I Lin, Mikhail Y. Shalaginov, Katherine Stoll, Sensong An, Clara Rivero-Baleine, Myungkoo Kang, Anuradha Agarwal, Kathleen Richardson, Hualiang Zhang, Juejun Hu, and Tian Gu**

Zoom lenses with variable focal lengths and magnification ratios are essential for many optical imaging applications. Conventional zoom lenses are composed of multiple refractive optics, and optical zoom is attained via translational motion of one or more lens elements, which adds to module size, complexity, and cost. In this paper, a zoom lens design based on multi-functional optical metasurfaces is presented, which achieves large step zoom ratios, minimal distortion, and diffraction-limited optical quality without requiring mechanical moving parts. Two embodiments of the concept are experimentally demonstrated based on polarization-multiplexing in the visible and phase change materials in the mid-infrared, both yielding 10× parfocal zoom in accordance with the design.

1. Introduction

Zoom lenses with adjustable effective focal length (EFL) and magnification ratio are widely employed in applications spanning photography, cinematography, computer vision, biomedical imaging, microscopy, image projection, and beyond. Traditionally, optical zoom is realized by switching between multiple lens groups, each with a fixed zoom (e.g., in most phone cameras); or using stacked lenses where one or more of the lens elements move along the optical axis.[1–3] Both approaches, however, come at the cost of size, weight, complexity, cost, and sometimes image quality. Lenses made of liquids or elastomers have also been introduced to achieve zoom via shape deformation,[4–8] although concerns over reliability, controllability, optical quality, and scalability still loom.

Metasurfaces, flat optical components which control phase, amplitude, and polarization states of light with sub-wavelength structures, have been gaining increasing traction.[9–19] Active metasurfaces, whose optical functionalities can be dynamically modulated, further enable tuning of metalens focal length via mechanisms including substrate deformation,[20–24] microelectromechanical systems (MEMS) actuation,[25,26] thermo-optic effect,[27] polarization multiplexing,[28–31] as well as phase transition in materials.[32–34] Optical zoom, however, is a more complex function that has largely remained unexplored in metasurface optics. While a number of "zoom metalens" designs have been proposed,[24,35–38] they are in fact varifocal lenses[25,27,39–53] whose focal plane constantly shifts as the lens configuration changes. A true zoom metalens must be parfocal; in other words, the position of its focal plane must remain stationary when its EFL is changed. A parfocal zoom metalens design was first theoretically conceptualized by Zheng et al.[54,55] However, the design only affords a small zoom ratio. Moreover, no parfocal zoom metalens has been experimentally demonstrated to our knowledge.

In this paper, we propose a non-mechanical parfocal zoom metalens design offering large zoom ratios, minimal distortion, and aberration-free optical quality. As one specific example, the design can switch between 40° (the "wide-angle" mode) and 4° (the "telephoto" mode) field-of-view (FOV) with 10× optical zoom. The concept is generic with respect to meta-atom design, which we validated through implementation of two embodiments: a polarization-multiplexing zoom metalens in the visible using waveguide-type meta-atoms; and a zoom metalens in the mid-infrared in the form of a reconfigurable Huygens' surface made of phase change materials (PCMs).

F. Yang, H.-I. Lin, M. Y. Shalaginov, K. Stoll, S. An, A. Agarwal, J. Hu, T. Gu
Department of Materials Science and Engineering
Massachusetts Institute of Technology
Cambridge, MA 02139, USA
E-mail: hujuejun@mit.edu; gutian@mit.edu

C. Rivero-Baleine
Missiles and Fire Control
Lockheed Martin Corporation
Orlando, FL 32819, USA

M. Kang, K. Richardson
The College of Optics and Photonics, Department of Materials Science and Engineering
University of Central Florida
Orlando, FL 32816, USA

A. Agarwal, T. Gu
Materials Research Laboratory
Massachusetts Institute of Technology
Cambridge, MA 02139, USA

H. Zhang
Department of Electrical and Computer Engineering
University of Massachusetts Lowell
Lowell, MA 01854, USA

The ORCID identification number(s) for the author(s) of this article can be found under https://doi.org/10.1002/adom.202200721.

DOI: 10.1002/adom.202200721

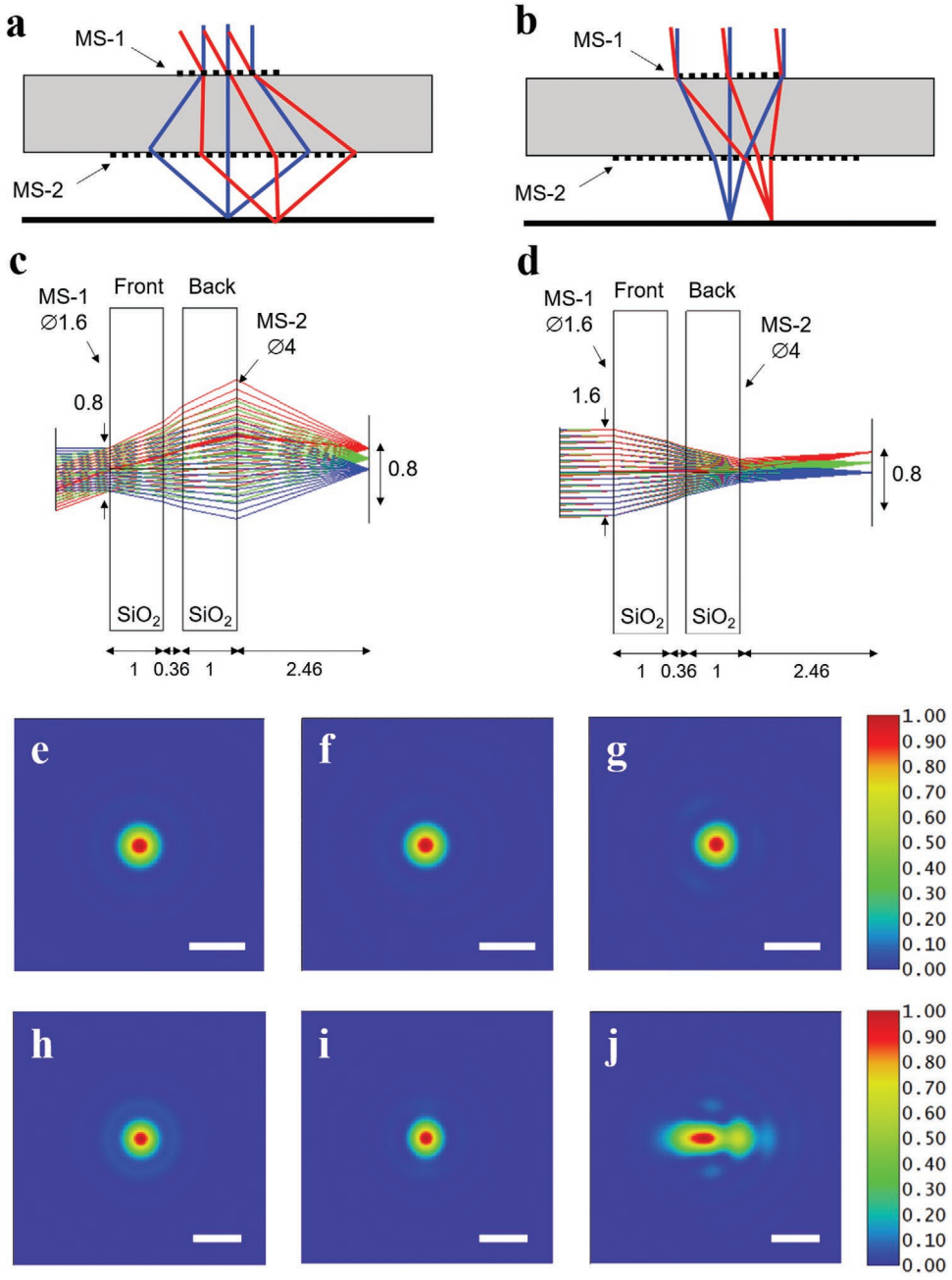

Figure 1. a,b) Schematic illustration of the doublet zoom metalens configuration in the wide-angle mode (a) and telephoto mode (b). MS-1 and MS-2 labels the front and back metasurfaces, respectively. Note that the optical aperture sizes are different in the two imaging modes and controlled by the metasurfaces via reconfigurable wavefront shaping. c,d) Ray trace simulation of the optimized polarization-multiplexed zoom metalens in the wide-angle mode (c) and telephoto mode (d). All the units are in mm. e–g) Simulated focal spot profiles in the wide-angle mode with the AOI of 0° (e), 10° (f), and 20° (g) (scale bars: 2 μm). h–j) Simulated focal spot profiles in the telephoto mode with the AOI of 0° (h), 1° (i), and 2° (j) (scale bars: 10 μm).

2. Zoom Metalens Design: The Concept

The zoom metalens assumes a doublet configuration as illustrated in **Figure 1**a,b. The two metasurfaces can be fabricated either on the opposite sides of a single substrate or on two separate substrates. Each metasurface encodes two different phase maps corresponding to two zoom states. In the wide-angle mode, the center part of the front metasurface serves as a negative lens which expands the incident light beam to a larger width on the back metasurface, and the back metasurface acts as a positive lens to form the image. The lens in this state therefore realizes a small EFL to accommodate a large FOV. In the telephoto mode, the front metasurface functions as a positive lens which focuses the incident light beam to a smaller area on

the back metasurface. The back metasurface instead becomes a negative lens to realize a larger EFL than the wide-angle mode while maintaining the same parfocal length. The zoom ratio is defined as the EFL of the telephoto mode divided by that of the wide-angle mode.

A key feature of the design that sets it apart from previous proposals is that the front metasurface not only acts as a tunable lens but also a variable aperture without involving mechanical moving parts. This is essential to achieving a large zoom ratio while suppressing aberrations. In the telephoto mode, the front aperture coincides with the metasurface area. The wide-angle mode, however, reduces the front aperture size by blocking light transmission in the outside ring. This can be accomplished either by imposing a phase profile with a large gradient to deflect and trap light via total internal reflection in the substrate (which is what we opted for in both visible and mid-IR zoom lens demonstrations), or engineering the meta-atoms such that they curtail optical transmission in the wide-angle state.

As an example to illustrate our design, here we consider the polarization-multiplexed zoom lens, which is designed for a target center wavelength of 670 nm. The lens comprises two 1 mm thick fused-silica substrates with an air-gap of 0.36 mm in between. The front metasurface has a diameter of 1.6 mm, and the back metasurface has a diameter of 4.0 mm. The back focal length has a fixed value of 2.46 mm with the maximum image height of 0.4 mm in both modes. The total track length of the lens is 4.82 mm. The phase profiles of the metasurfaces were numerically optimized by assuming an even order polynomials form

$$\phi(r) = \sum_{i=1}^{11} A_i \left(\frac{r}{R}\right)^{2i} \quad (1)$$

where R = 3 mm, r is the radial coordinate, and the A_i's are the polynomial coefficients. Figure 1c,d presents ray trace simulation results of the optimized lens. The details of the optimization process and the coefficients are presented in the Supporting Information. The lens exhibits an EFL of 1.1 mm (corresponding to an *f*-number of 1.4 and a numerical aperture NA = 0.34) in the wide-angle mode and 10.8 mm (*f*-number 6.8 and NA = 0.07) in the telephoto mode. Figures 1e–g and 1h–j show the simulated focal spot profiles of the lens, featuring diffraction-limited performance over the entire 40° FOV in the wide-angle mode and over a 3° FOV in the telephoto mode, with near-diffraction-limited performance as the angle-of-incidence (AOI) increases to ±2° for the later case. The distortion is less than 5% in both modes. The lens therefore furnishes high imaging quality and negligible distortion in both zoom modes with a large zoom ratio of 10×. Further performance improvements can be realized by engineering angle-dependent response of meta-atoms or resorting to non-local metasurface designs.[56]

3. Polarization-Multiplexed Metasurface Design

In this embodiment, the two zoom states are associated with two orthogonal linear polarizations of the incident light. The polarization-multiplexed meta-atom structure is schematically depicted in **Figure 2**a, which assumes the form of a truncated

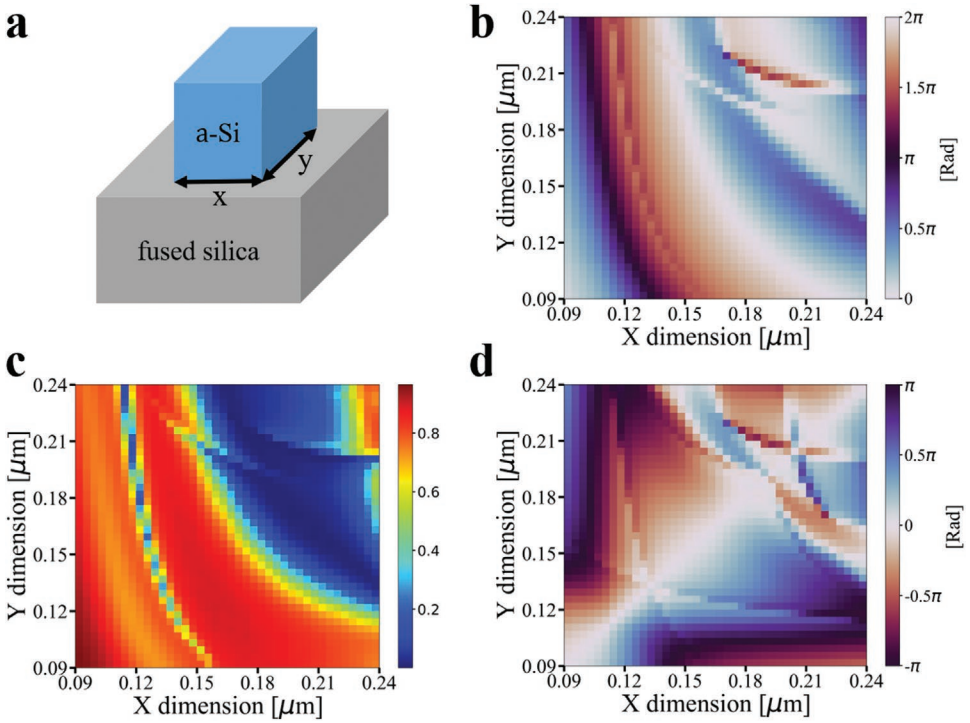

Figure 2. Polarization-multiplexed meta-atom design. a) Schematic illustration of the meta-atom structure. b) Phase delay and c) amplitude response of the meta-atoms with the polarization of the incident light along the *x*-direction. d) Phase delay difference of the meta-atoms between the *x* and *y* polarization directions.

rectangular waveguide made of amorphous Si (a-Si) sitting on a fused silica substrate. The meta-atoms have a unit-cell period of 0.3 μm with a height of 0.45 μm. The 670 nm wavelength incident light is linearly polarized along the x and y directions, parallel to the edges of the rectangular waveguide.

We simulated the meta-atom response with x-polarized light using the finite-difference time-domain (FDTD) method. Optical phase and amplitude imparted by meta-atoms with different lateral dimensions in the range of 90–240 nm are shown in Figure 2b,c. Response of the same meta-atom to y-polarized light can be directly inferred from the same data by swapping the x and y dimensions. The meta-atoms can cover the entire $0–2\pi$ phase range for the two polarizations. Birefringence of the truncated waveguide with respect to the two orthogonal linear polarization states controls the optical phase difference in two states. Figure 2d plots the phase delay difference between the two polarizations imposed by the meta-atoms, showing that the relative phase delay covers the entire range of $\pm\pi$, sufficient to provide arbitrarily reconfigurable phase profiles for both polarizations.

To construct the zoom lens, we chose 16 meta-atoms (i.e., a 2-bit design[33]) from the simulated meta-atom library to cover four phase levels of 0, $\pi/2$, π, and $3\pi/2$, with each meta-atom providing a distinct combination of two of the four discrete phase values for the two polarization states. As a result, the phase profiles of the metasurface can be independently controlled in response to the two polarizations. The selected meta-atom structures as well as their phase and amplitude responses are listed in the Supporting Information. All meta-atoms have transmittance larger than 70%.

4. Polarization-Multiplexed Metalens Fabrication, Characterization, and Imaging Demonstration

The metasurfaces were defined using electron beam lithography and plasma etching. Details of the fabrication process are discussed in Section 7. **Figure 3**a,b shows scanning electron microscope (SEM) images of the fabricated metasurfaces. After metasurface fabrication, metal apertures were patterned on the substrates, only exposing areas with the metasurfaces to eliminate unwanted stray light transmission (Figure 3c,e).

To characterize the metalens assembled from the two pieces of substrate, we started with evaluating the focal spot profiles of the zoom lens in the two polarization states. The measurement setup is illustrated in **Figure 4**a. A 670 nm laser along with a collimator were both mounted on a custom-made circular track to adjust the AOI within the range of −20° to 20°. The focal spot was magnified by a pair of lenses forming a telescope assembly and captured by a CMOS image sensor. A polarizer was placed in between the laser and the zoom lens to control the polarization state of the incident light. The focal spot images and the normalized cross-sectional optical intensity profiles at different AOIs and polarization states are presented in Figure 4b–m alongside the focal spot profiles of an ideal, aberration-free lens of the same aperture size and effective f-number. The Strehl ratios can be inferred from the peak value of the focal spot profiles. The full-width-at-half-maximum (FWHM) of the focal spots are summarized in **Table 1**, showing agreement between the simulation and experimental results. We further quantified the focusing efficiency of the zoom lens, which is defined as the ratio of optical power at the focal spot to the total power incident on the lens aperture. The focusing efficiency was assessed using a photodetector integrated with a 100 μm diameter pinhole. Our measurement indicated focusing efficiencies of 8% at the wide-angle mode and 14% at the telephoto mode of the doublet zoom lens.

We used a similar setup to characterize the imaging performance of the zoom lens in two modes. A printed white board containing standard USAF resolution chart patterns and different sizes of "MIT" characters was placed 0.5 m away from the zoom lens. An LED light source with 660 nm center wavelength and 20 nm FWHM spectral bandwidth was used to illuminate the object. The image was magnified using the telescope assembly and captured by the image sensor. A polarizer is placed in front of the sensor to control the imaging mode of the zoom lens. The images of the object in the two polarization states are shown in **Figure 5**a–f, indicating excellent image

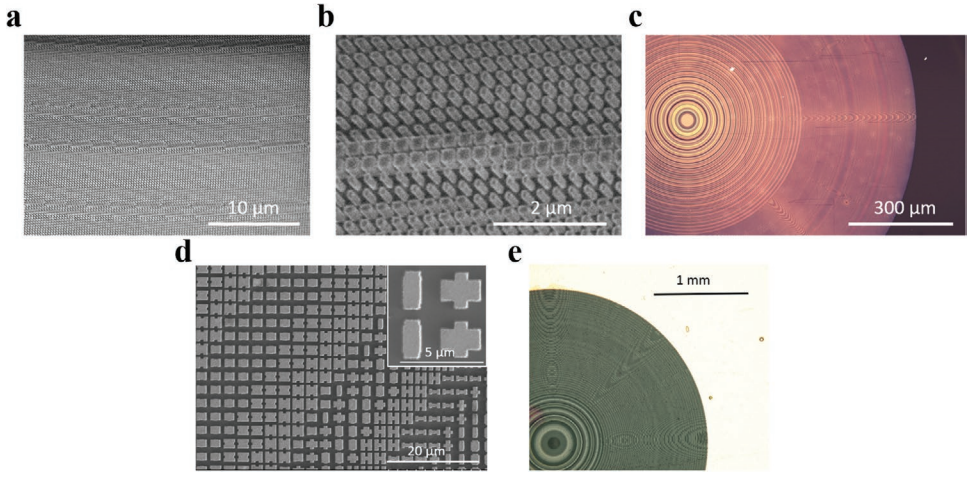

Figure 3. Fabricated metalenses. a,b) SEM images and c) optical microscope (OM) image of the polarization-multiplexed metalens. d) SEM image and e) OM image of the phase-change metalens.

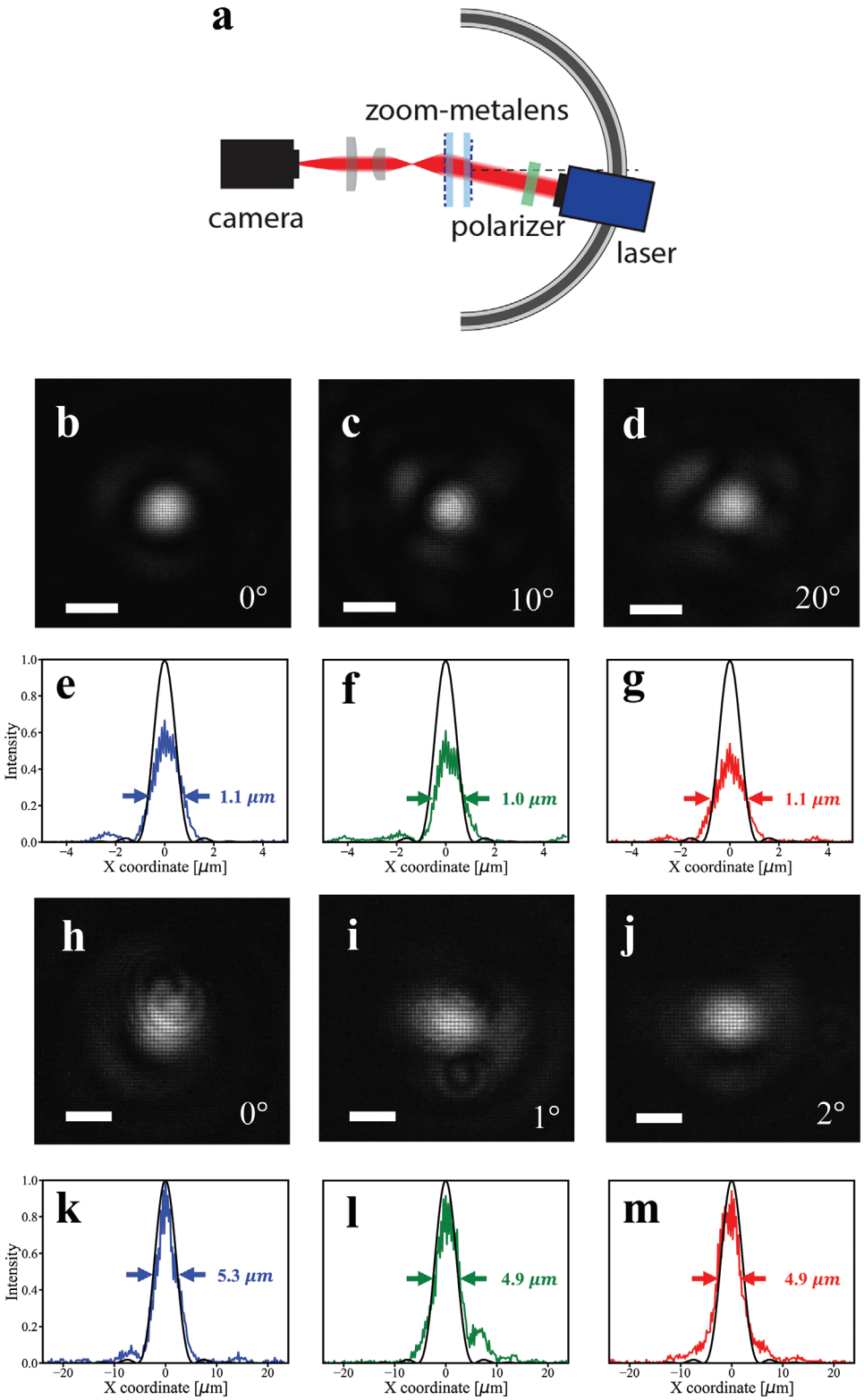

Figure 4. Focal spot characterization. a) Schematic illustration of the measurement setup. b–d) Focal spots at various AOIs in the 40° FOV wide-angle mode (scale bars: 2 µm). e–g) Normalized intensity distributions of the focal spots on the focal plane at AOIs of 0° (e), 10° (f), and 20° (g) in the wide-angle mode. h–j) Focal spots at various AOIs in the 4° FOV telephoto mode (scale bars: 5 µm). k–m) Normalized intensity distributions of the focal spots on the focal plane at AOIs of 0° (k), 1° (l), and 2° (m) in the telephoto mode. The color lines are from the measurement and the black lines are from an ideal aberration-free lens with the same NA. Their peak intensities are normalized to have the same power within an area of a diameter equaling to five times the focal spot FWHM.

Table 1. FWHM of the focal spots of the polarization-multiplexed metalens.

Mode	Wide-angle (sagittal/tangential)			Telephoto (sagittal/tangential)		
AOI [°]	0	10	20	0	1.0	2.0
FWHM [μm] (simulation)	1.0/1.0	1.0/1.0	1.0/1.0	4.8/4.8	4.7/4.8	3.9/9.5
FWHM [μm] (experiment)	1.1/1.1	0.8/1.0	1.0/1.1	5.3/5.3	4.9/4.9	4.5/4.9

quality in both states with negligible cross-talk, and a measured magnification ratio of 9.6×. The slight deviation from the 10× design target is likely due to the slight deviations of the air-gap thickness and image plane position from the design.

5. Phase-Change Reconfigurable Zoom Metalens

To demonstrate that our zoom metalens architecture is agnostic to meta-atom type, the design was also implemented with a PCM-based reconfigurable Huygens' surface at 5.2 μm wavelength capitalizing on the giant refractive index change accompanying amorphous-crystalline structural transformation in chalcogenide PCMs.[32,57–70] **Figure 6**a–f illustrates the design and modeled focal spot profiles of the lens. Similar to the polarization-multiplexed counterpart, the lens also comprises of two metasurfaces patterned on two mid-IR transparent CaF_2 substrates separated by an air gap. The lens performance is summarized in **Table 2**. The meta-atoms were patterned in $Ge_2Sb_2Se_4Te$[71,72] (GSST), a PCM which exhibits low optical losses at 5.2 μm wavelength. The metasurfaces are constructed from a library of pre-selected meta-atoms with "H", "I", and "+" shapes (see Supporting Information for details), which we have shown to support multiple electric and magnetic resonances, thereby providing broad optical phase coverage.[73,74] The meta-atom designs were quantitatively evaluated using a performance figure-of-merit (FOM) accounting for both transmission amplitude and phase error,[34] and optimal meta-atom geometries with maximum FOM values were selected to assemble the metasurfaces. The final meta-atom selections are summarized in the Supporting Information.

Fabrication protocols of the PCM metasurfaces were elaborated in Section 7 and Figure 3d,e presents top-view SEM and optical micrographs of the GSST metasurface. Quantitative analysis of the SEM images taken on the metasurface revealed excellent pattern fidelity of the meta-atoms, with an average size deviation of only 20 nm from design values. The etched GSST meta-atoms have almost vertical sidewall profiles with a sidewall angle of 86°. The as-fabricated meta-atoms reside in an amorphous structural state. Structural phase transition (amorphous to crystalline) was triggered by annealing the metasurfaces on a hot plate at 250 °C and in an inert gas ambient for 30 min. While here we used thermal annealing to demonstrate switching operation of the prototype, the design concept can also be adapted to reversible electrothermal switching using on-chip micro-heaters to enable compact optics integration.[70,75]

Figure 6 presents ray trace simulation results of the optimized lens and the simulated focal spot profiles. The focusing performance of the lens was measured using a setup similar to that used for the visible zoom metalens. A 5.2 μm collimated laser beam incident at various angles, ranging from −20° to 20° in the amorphous state and −2° to 2° in the crystalline states, served as a far-field light source. Focal spot images were magnified using a telescope assembly and projected onto a liquid nitrogen cooled InSb focal plane array. The recorded focal spots form a crisp image, thereby verifying the change in observed FOVs and the target 10× zoom (**Figure 7**).

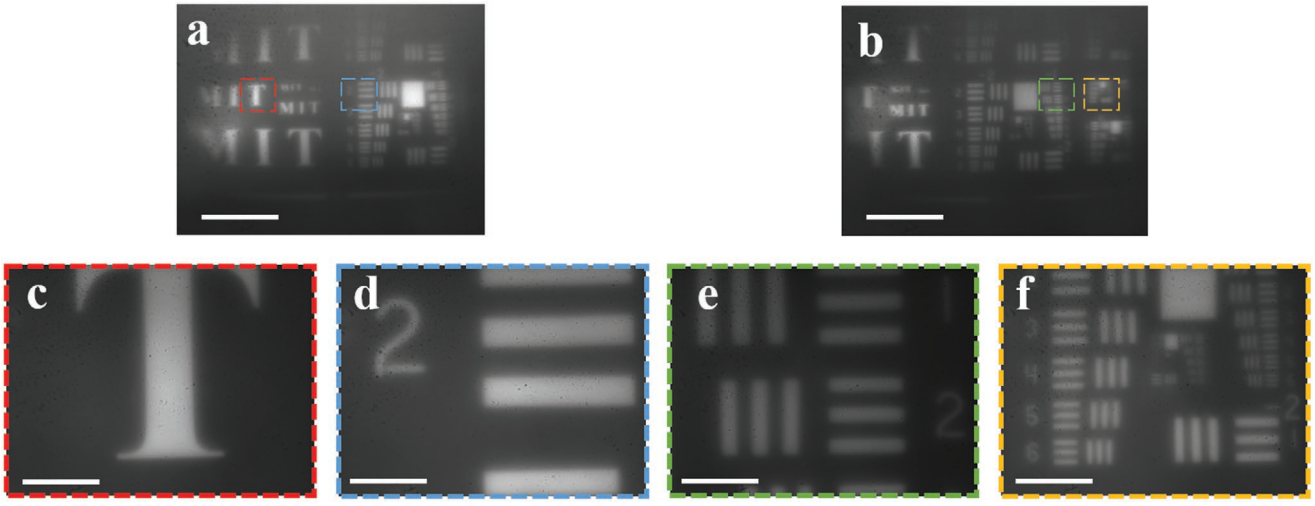

Figure 5. Experimental demonstration of zoom imaging. Images captured by the zoom metalens in the a,b) wide-angle mode (scale bars: 10° FOV) and c–f) telephoto mode (scale bars: 1° FOV).

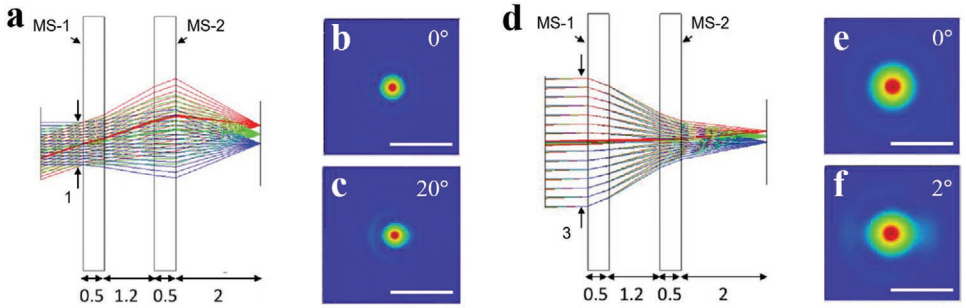

Figure 6. a) Ray trace simulation and b,c) focal spot profiles of the phase-change reconfigurable zoom metalens in the wide-angle mode. d) Ray trace simulation and e,f) focal spot profiles in the telephoto mode. (All the units are in mm, the scale bars are 30 μm).

6. Conclusion

We proposed a non-mechanical zoom lens architecture offering large zoom ratios, negligible distortion, and diffraction-limited performance. Leveraging this generic architecture, two zoom metalenses designs were developed and experimentally realized, using polarization-multiplexed and phase-change metasurfaces to achieve optical zoom at visible and mid-IR wavelengths, respectively. While both prototypes are monochromatic, dispersion-engineered metasurface designs can potentially be adopted to further empower the zoom lenses with multi-color or even broadband functions.[76–83] The versatile, multi-functional zoom metalens platform features a compact form factor, excellent image quality, and no mechanical moving parts, thereby foreseeing new applications in microscopy, optical sensing, image projection, and medical imaging.

7. Experimental Section

Polarization-Multiplexed Metalens Fabrication: A 450 nm thick amorphous Si film was deposited on a 0.5 mm thick fused silica wafer by plasma-enhanced chemical vapor deposition (STS PECVD). The wafer was then diced into square pieces with side length of 12.5 mm as metalens substrates. To fabricate the mask patterns of metalens, a negative tone of electron beam resist (ma-N 2402 from a mixture of ma-N 2401 and ma-N 2403, Micro Resist Technology) and then a conductive polymer (ESpacer 300Z, Showa Denko America, Inc.) were spin-coated on the substrates for electron beam lithography (EBL). The use of a conductive polymer avoids charging effects during EBL writing. The EBL was conducted at a voltage of 50 kV and a beam current of 1 nA (Elionix HS50). Then, the sample was put in the developer (AZ 726 MIF Developer) to produce the mask patterns and gently rinsed with deionized water. To etch amorphous Si, the dry-etching was performed by dual plasma sources and dual gas inlets with a mixture of SF_6 and C_4F_8 (SPTS Rapier DRIE). Residual electron beam resist was stripped by O_2 plasma ashing. Areas on the substrate not occupied by the metasurface were subsequently covered by a metal mask to prevent stray light. To fabricate the metal mask, a negative-tone photoresist (AZ nLOF 2035) was spin-coated on the metalens at 3000 rpm. The resist was soft baked at 115 °C for 1 min, exposed to UV light on a MLA150 Maskless Aligner, and then post-exposure baked at 115 °C for 1 min. The photoresist was developed by immersing the sample into Microposit MF-319 developer for 1 min and gently rinsed with deionized water. Then, a 200 nm thick Cr layer was deposited by electron beam evaporation at a rate of 2.0 Å s^{-1} in a Sharon electron beam evaporator. Finally, the photoresist was removed in solvent stripper (Remover PG, MicroChem) to pattern the metal mask via lift-off.

Phase-Change Metalens Fabrication: GSST films were deposited onto a double-side polished CaF_2 (111) substrate (MTI Corp.) by single-source thermal evaporation in a custom-made system (PVD Products Inc.).[84] The substrate was held near room temperature throughout the film deposition process. Thickness of the film was measured with a stylus profilometer (Bruker DXT) to be 1.09 μm (a-state) and 1.03 μm (c-state), indicating 5% volumetric contraction during crystallization similar to other phase-change materials.[85,86] The film was patterned via EBL on an Elionix ELS-F125 system followed by reactive ion etching (Plasmatherm, Shuttlelock System VII SLR-770/734). The electron beam writing was carried out on an 800-nm-thick layer of ZEP520A resist, which was spin coated on top of the GSST film at 2000 rpm for 1 min and then baked at 180 °C for 1 min. To avoid the difficulty of ZEP removal after the etching step, a thin layer (about 200 nm) of 495 PMMA A4 between GSST and ZEP was introduced by spin-coating the photoresist at 4000 rpm and then baking it at 180 °C for 1 min. Before resist coating, the GSST surface was mildly treated with standard oxygen plasma cleaning to improve resist adhesion. To prevent charging effects during the electron beam writing process, the resist was covered with a water-soluble conductive polymer (ESpacer 300Z, Showa Denko America, Inc.).[87] The EBL writing was performed with a voltage of 125 kV, 120 μm aperture, and 10 nA writing current. Proximity error correction was also implemented with a base dose time of 0.03 μsdot^{-1} (which corresponds to a dosage of 300 μ C cm^{-2}). The exposed photoresist was developed by subsequently immersing the sample into water, ZED-N50 (ZEP developer), and isopropanol for 1 min each. Reactive ion etching was performed with a gas mixture of CHF_3:CF_4 (3:1) with respective flow rates of 45 and 15 sccm, pressure of 10 mTorr, and RF power of 200 W. The etching rate was 80 nmmin^{-1}. The etching was done in three cycles of 5 min with cooldown breaks of several minutes in between. After completing the etching step, the sample was soaked in *N*-methyl-2-pyrrolidone overnight to remove the residual ZEP resist mask. After optical characterization of the metalens in the amorphous (as-deposited) state, the sample was transitioned to the crystalline state by hot-plate annealing at 250 °C for 30 min. The annealing was conducted in a glovebox filled with an

Table 2. FWHM of the focal spots of the phase-change reconfigurable zoom metalens.

Mode	Wide-angle (sagittal/tangential)					Telephoto (sagittal/tangential)				
AOI [°]	0	5	10	15	20	0	0.5	1.0	1.5	2.0
FWHM [μm] (simulation)	7.3/7.3	7.3/7.4	7.3/7.3	7.1/7.3	7.2/7.6	14.9/14.9	14.9/15.1	14.9/15.1	15.0/15.4	14.4/18.4
FWHM [μm] (experiment)	4.8/6.0	5.5/7.3	5.8/6.8	6.3/10.3	7.3/7.3	12.8/9.0	12.5/9.8	14.3/9.5	15.0/12.3	9.5/19.5

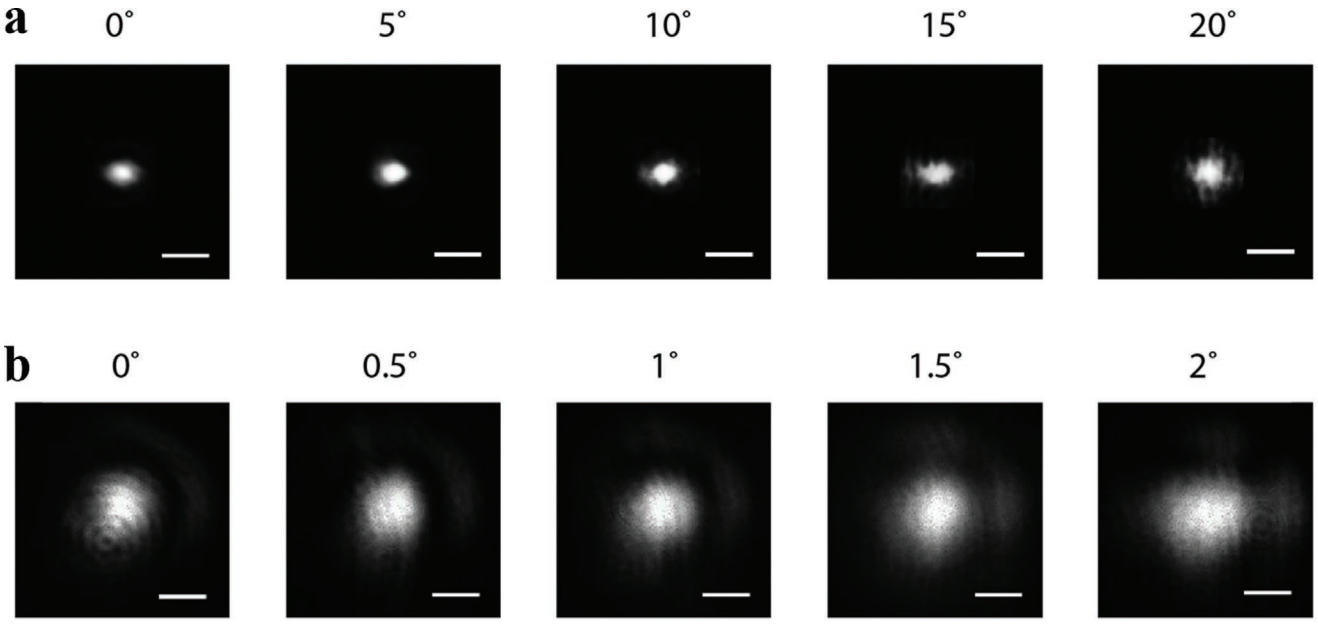

Figure 7. Focal spot profiles of the phase-change reconfigurable zoom metalens at different AOIs in the a) wide-angle mode and b) telephoto mode. (The scale bars are 20 μm).

ultra-high purity argon atmosphere. By using the lift-off technique described above, 200-nm-thick gold apertures was lithographically defined around the metasurfaces.

Supporting Information

Supporting Information is available from the Wiley Online Library or from the author.

Acknowledgements

F.Y., H.-I.L., and M.Y.S. contributed equally to this work. This work was funded by Defense Advanced Research Projects Agency Defense Sciences Office Program: EXTREME Optics and Imaging (EXTREME) under agreement no. HR00111720029 and by the MIT Skoltech Seed Fund Program. The authors acknowledge characterization facility support provided by the Materials Research Laboratory at Massachusetts Institute of Technology (MIT), as well as fabrication facility support by MIT.nano and the Center for Nanoscale Systems at Harvard University. The views, opinions, and/or findings expressed are those of the authors and should not be interpreted as representing the official views or policies of the Department of Defense or the U.S. Government.

Conflict of Interest

The authors declare no conflict of interest.

Data Availability Statement

The data that support the findings of this study are available in the Supporting Information of this article.

Keywords

metalens, metasurfaces, parfocal lens, phase change materials, polarization, reconfigurable optics, zoom lens

Received: March 27, 2022
Revised: April 29, 2022
Published online:

[1] K. Tanaka, *Appl. Opt.* **1982**, *21*, 2174.
[2] R. B. Johnson, C. Feng, *Appl. Opt.* **1992**, *31*, 2274.
[3] M. Demenikov, E. Findlay, A. R. Harvey, *Opt. Express* **2009**, *17*, 6118.
[4] S. Shian, R. M. Diebold, D. R. Clarke, *Opt. Express* **2013**, *21*, 8669.
[5] N. Sugiura, S. Morita, *Appl. Opt.* **1993**, *32*, 4181.
[6] N. Chronis, G. L. Liu, K.-H. Jeong, L. P. Lee, *Opt. Express* **2003**, *11*, 2370.
[7] S. Lee, M. Choi, E. Lee, K.-D. Jung, J.-h. Chang, W. Kim, *Opt. Express* **2013**, *21*, 1751.
[8] M. Ye, M. Noguchi, B. Wang, S. Sato, *Electron. Lett.* **2009**, *45*, 646.
[9] N. Yu, P. Genevet, M. A. Kats, F. Aieta, J.-P. Tetienne, F. Capasso, Z. Gaburro, *Science* **2011**, *334*, 333.
[10] F. Capasso, *Nanophotonics* **2018**, *7*, 953.
[11] K. Achouri, C. Caloz, *Nanophotonics* **2018**, *7*, 1095.
[12] S. M. Kamali, E. Arbabi, A. Arbabi, A. Faraon, *Nanophotonics* **2018**, *7*, 1041.
[13] P. R. West, J. L. Stewart, A. V. Kildishev, V. M. Shalaev, V. V. Shkunov, F. Strohkendl, Y. A. Zakharenkov, R. K. Dodds, R. Byren, *Opt. Express* **2014**, *22*, 26212.
[14] P. Lalanne, P. Chavel, *Laser Photonics Rev.* **2017**, *11*, 1600295.
[15] M. L. Tseng, H.-H. Hsiao, C. H. Chu, M. K. Chen, G. Sun, A.-Q. Liu, D. P. Tsai, *Adv. Opt. Mater.* **2018**, *6*, 1800554.
[16] A. V. Kildishev, A. Boltasseva, V. M. Shalaev, *Science* **2013**, *339*, 1232009.
[17] S. B. Glybovski, S. A. Tretyakov, P. A. Belov, Y. S. Kivshar, C. R. Simovski, *Phys. Rep.* **2016**, *634*, 1.

[18] X. Ni, Z. J. Wong, M. Mrejen, Y. Wang, X. Zhang, *Science* **2015**, *349*, 1310.
[19] H. Chu, X. Xiong, Y.-J. Gao, J. Luo, H. Jing, C.-Y. Li, R. Peng, M. Wang, Y. Lai, *Sci. Adv.* **2021**, *7*, eabj0935.
[20] H.-S. Ee, R. Agarwal, *Nano Lett.* **2016**, *16*, 2818.
[21] S. M. Kamali, E. Arbabi, A. Arbabi, Y. Horie, A. Faraon, *Laser Photonics Rev.* **2016**, *10*, 1002.
[22] S. C. Malek, H.-S. Ee, R. Agarwal, *Nano Lett.* **2017**, *17*, 3641.
[23] F. Cheng, L. Qiu, D. Nikolov, A. Bauer, J. P. Rolland, A. N. Vamivakas, *Opt. Express* **2019**, *27*, 15194.
[24] S. Wei, G. Cao, H. Lin, X. Yuan, M. Somekh, B. Jia, *ACS Nano* **2021**, *15*, 4769.
[25] S. Colburn, A. Zhan, A. Majumdar, *Optica* **2018**, *5*, 825.
[26] A. She, S. Zhang, S. Shian, D. R. Clarke, F. Capasso, *Sci. Adv.* **2018**, *4*, eaap9957.
[27] A. Afridi, J. Canet-Ferrer, L. Philippet, J. Osmond, P. Berto, R. Quidant, *ACS Photonics* **2018**, *5*, 4497.
[28] D. Wen, F. Yue, G. Li, G. Zheng, K. Chan, S. Chen, M. Chen, K. F. Li, P. W. H. Wong, K. W. Cheah, E. Y. B. Pun, S. Zhang, X. Chen, *Nat. Commun.* **2015**, *6*, 8241.
[29] C. Guan, J. Liu, X. Ding, Z. Wang, K. Zhang, H. Li, M. Jin, S. N. Burokur, Q. Wu, *Nanophotonics* **2020**, *9*, 3605.
[30] W. Wang, R. Zhao, S. Chang, J. Li, Y. Shi, X. Liu, J. Sun, Q. Kang, K. Guo, Z. Guo, *Nanomaterials* **2021**, *11*, 1485.
[31] W. Wang, Q. Yang, S. He, Y. Shi, X. Liu, J. Sun, K. Guo, L. Wang, Z. Guo, *Opt. Express* **2021**, *29*, 43270.
[32] X. Yin, T. Steinle, L. Huang, T. Taubner, M. Wuttig, T. Zentgraf, H. Giessen, *Light: Sci. Appl.* **2017**, *6*, e17016.
[33] M. Y. Shalaginov, S. D. Campbell, S. An, Y. Zhang, C. Ríos, E. B. Whiting, Y. Wu, L. Kang, B. Zheng, C. Fowler, H. Zhang, D. H. Werner, J. Hu, T. Gu, *Nanophotonics* **2020**, *9*, 3505.
[34] M. Y. Shalaginov, S. An, Y. Zhang, F. Yang, P. Su, V. Liberman, J. B. Chou, C. M. Roberts, M. Kang, C. Rios, Q. Du, C. Fowler, A. Agarwal, K. A. Richardson, C. Rivero-Baleine, H. Zhang, J. H. T. Gu, *Nat. Commun.* **2021**, *12*, 1225.
[35] Y. Wei, Y. Wang, X. Feng, S. Xiao, Z. Wang, T. Hu, M. Hu, J. Song, M. Wegener, M. Zhao, J. Xia, Z. Yang, *Adv. Opt. Mater.* **2020**, *8*, 2000142.
[36] Y. Cui, G. Zheng, M. Chen, Y. Zhang, Y. Yang, J. Tao, T. He, Z. Li, *Chin. Opt. Lett.* **2019**, *17*, 111603.
[37] N. Xu, Y. Hao, K. Jie, S. Qin, H. Huang, L. Chen, H. Liu, J. Guo, H. Meng, F. Wang, X. Yang, Z. Wei, *Nanomaterials* **2021**, *11*, 729.
[38] C. Wang, Y. Sun, Q. Zhang, Z. Yu, C. Tao, J. Zhang, F. Wu, R. Wu, Z. Zheng, *Opt. Express* **2021**, *29*, 26569.
[39] Z. Liu, Z. Du, B. Hu, W. Liu, J. Liu, Y. Wang, *JOSA B* **2019**, *36*, 2810.
[40] M. D. Aiello, A. S. Backer, A. J. Sapon, J. Smits, J. D. Perreault, P. Llull, V. M. Acosta, *ACS Photonics* **2019**, *6*, 2432.
[41] Y. Guo, M. Pu, X. Ma, X. Li, R. Shi, X. Luo, *Appl. Phys. Lett.* **2019**, *115*, 163103.
[42] Y. Luo, C. H. Chu, S. Vyas, H. Y. Kuo, Y. H. Chia, M. K. Chen, X. Shi, T. Tanaka, H. Misawa, Y.-Y. Huang, D. P. Tsai, *Nano Lett.* **2021**, *21*, 5133.
[43] C.-Y. Fan, T.-J. Chuang, K.-H. Wu, G.-D. J. Su, *Opt. Express* **2020**, *28*, 10609.
[44] S. Qin, N. Xu, H. Huang, K. Jie, H. Liu, J. Guo, H. Meng, F. Wang, X. Yang, Z. Wei, *Opt. Express* **2021**, *29*, 7925.
[45] S. Zarei, A. Khavasi, *IEEE Access* **2021**, *9*, 73453.
[46] Y. Wang, L. Chen, S. Tang, P. Xu, F. Ding, Z. Fang, A. Majumdar, *Opt. Express* **2021**, *29*, 39461.
[47] K. Iwami, C. Ogawa, T. Nagase, S. Ikezawa, *Opt. Express* **2020**, *28*, 35602.
[48] F. Balli, M. A. Sultan, J. T. Hastings, *Opt. Lett.* **2021**, *46*, 3548.
[49] M. Bosch, M. R. Shcherbakov, K. Won, H.-S. Lee, Y. Kim, G. Shvets, *Nano Lett.* **2021**, *21*, 3849.
[50] Y. Chen, S. Pu, C. Wang, F. Yi, *Opt. Lett.* **2021**, *46*, 1930.
[51] S. Colburn, A. Majumdar, *ACS Photonics* **2019**, *7*, 120.
[52] C. Ogawa, S. Nakamura, T. Aso, S. Ikezawa, K. Iwami, *Nanophotonics* **2022**, *11*, 1941.
[53] A. Archetti, R.-J. Lin, T. V. Tsoulos, F. Kiani, N. Restori, G. Tagliabue, in *Current Developments in Lens Design and Optical Engineering XXII*, Vol. *11814*, (Eds: R. B. Johnson, V. N. Mahajan, S. Thibault), International Society for Optics and Photonics, Bellingham, WA **2021**, p. 1181407.
[54] G. Zheng, W. Wu, Z. Li, S. Zhang, M. Q. Mehmood, P. He, S. Li, *Opt. Lett.* **2017**, *42*, 1261.
[55] R. Fu, Z. Li, G. Zheng, M. Chen, Y. Yang, J. Tao, L. Wu, Q. Deng, *Opt. Express* **2019**, *27*, 12221.
[56] K. Shastri, F. Monticone, arXiv:2204.09154, **2022**.
[57] Q. Wang, E. T. Rogers, B. Gholipour, C.-M. Wang, G. Yuan, J. Teng, N. I. Zheludev, *Nat. Photonics* **2016**, *10*, 60.
[58] B. Gholipour, J. Zhang, K. F. MacDonald, D. W. Hewak, N. I. Zheludev, *Adv. Mater.* **2013**, *25*, 3050.
[59] Y. Wang, P. Landreman, D. Schoen, K. Okabe, A. Marshall, U. Celano, H.-S. P. Wong, J. Park, M. L. Brongersma, *Nat. Nanotechnol.* **2021**, *16*, 667.
[60] C. Williams, N. Hong, M. Julian, S. Borg, H. J. Kim, *Opt. Express* **2020**, *28*, 10583.
[61] F. Yue, R. Piccoli, M. Y. Shalaginov, T. Gu, K. A. Richardson, R. Morandotti, J. Hu, L. Razzari, *Laser Photonics Rev.* **2021**, *15*, 2000373.
[62] D. Sahoo, R. Naik, *Mater. Res. Bull.* **2021**, *148*, 111679.
[63] Y. Zhang, C. Ríos, M. Y. Shalaginov, M. Li, A. Majumdar, T. Gu, J. Hu, *Appl. Phys. Lett.* **2021**, *118*, 210501.
[64] M. N. Julian, C. Williams, S. Borg, S. Bartram, H. J. Kim, *Optica* **2020**, *7*, 746.
[65] C. R. de Galarreta, I. Sinev, A. M. Alexeev, P. Trofimov, K. Ladutenko, S. G.-C. Carrillo, E. Gemo, A. Baldycheva, J. Bertolotti, C. D. Wright, *Optica* **2020**, *7*, 476.
[66] A. Tittl, A.-K. U. Michel, M. Schäferling, X. Yin, B. Gholipour, L. Cui, M. Wuttig, T. Taubner, F. Neubrech, H. Giessen, *Adv. Mater.* **2015**, *27*, 4597.
[67] S. Abdollahramezani, O. Hemmatyar, M. Taghinejad, H. Taghinejad, A. Krasnok, A. A. Eftekhar, C. Teichrib, S. Deshmukh, M. El-Sayed, E. Pop, M. Wuttig, A. Alu, W. Cai, A. Adibi, arXiv:2104.10381, **2021**.
[68] C. Wu, H. Yu, S. Lee, R. Peng, I. Takeuchi, M. Li, *Nat. Commun.* **2021**, *12*, 96.
[69] J. Thompson, J. Burrow, P. Shah, J. Slagle, E. Harper, A. Van Rynbach, I. Agha, M. Mills, *Opt. Express* **2020**, *28*, 24629.
[70] Y. Zhang, C. Fowler, J. Liang, B. Azhar, M. Y. Shalaginov, S. Deckoff-Jones, S. An, J. B. Chou, C. M. Roberts, V. Liberman, M. Kang, C. Ríos, K. A. Richardson, C. Rivero-Baleine, T. Gu, H. Zhang, J. Hu, *Nat. Nanotechnol.* **2021**, *16*, 661.
[71] Q. Zhang, Y. Zhang, J. Li, R. Soref, T. Gu, J. Hu, *Opt. Lett.* **2018**, *43*, 94.
[72] Y. Zhang, J. B. Chou, J. Li, H. Li, Q. Du, A. Yadav, S. Zhou, M. Y. Shalaginov, Z. Fang, H. Zhong, C. Roberts, P. Robinson, B. Bohlin, C. Ríos, H. Lin, M. Kang, T. Gu, J. Warner, V. Liberman, K. Richardson, J. Hu, *Nat. commun.* **2019**, *10*, 4279.
[73] L. Zhang, J. Ding, H. Zheng, S. An, H. Lin, B. Zheng, Q. Du, G. Yin, J. Michon, Y. Zhang, Z. Fang, M. Y. Shalaginov, L. Deng, T. Gu, H. Zhang, J. Hu, *Nat. Commun.* **2018**, *9*, 1481.
[74] M. Y. Shalaginov, S. An, F. Yang, P. Su, D. Lyzwa, A. M. Agarwal, H. Zhang, J. Hu, T. Gu, *Nano Lett.* **2020**, *20*, 7429.
[75] C. Ríos, Y. Zhang, M. Y. Shalaginov, S. Deckoff-Jones, H. Wang, S. An, H. Zhang, M. Kang, K. A. Richardson, C. Roberts, J. B. Chou, V. Liberman, S. A. Vitale, J. Kong, T. Gu, J. Hu, *Adv. Photonics Res.* **2021**, *2*, 2000034.
[76] S. Wang, P. C. Wu, V.-C. Su, Y.-C. Lai, M.-K. Chen, H. Y. Kuo, B. H. Chen, Y. H. Chen, T.-T. Huang, J.-H. Wang, R.-M. Lin,

C.-H. Kuan, T. Li, Z. Wang, S. Zhu, D. P. Tsai, *Nat. Nanotechnol.* **2018**, *13*, 227.
[77] Q. Cheng, M. Ma, D. Yu, Z. Shen, J. Xie, J. Wang, N. Xu, H. Guo, W. Hu, S. Wang, T. Li, S. Zhuang, *Sci. Bull.* **2019**, *64*, 1525.
[78] A. Ndao, L. Hsu, J. Ha, J.-H. Park, C. Chang-Hasnain, B. Kanté, *Nat. Commun.* **2020**, *11*, 3205.
[79] F. Yang, S. An, M. Y. Shalaginov, H. Zhang, C. Rivero-Baleine, J. Hu, T. Gu, *Opt. Lett.* **2021**, *46*, 5735.
[80] Z. Li, P. Lin, Y.-W. Huang, J.-S. Park, W. T. Chen, Z. Shi, C.-W. Qiu, J.-X. Cheng, F. Capasso, *Sc. Adv.* **2021**, *7*, eabe4458.
[81] Z. Lin, C. Roques-Carmes, R. E. Christiansen, M. Soljačić, S. G. Johnson, *Appl. Phys. Lett.* **2021**, *118*, 041104.
[82] Z. Huang, M. Qin, X. Guo, C. Yang, S. Li, *Opt. Express* **2021**, *29*, 13542.
[83] E. Tseng, S. Colburn, J. Whitehead, L. Huang, S.-H. Baek, A. Majumdar, F. Heide, *Nat. Commun.* **2021**, *12*, 6493.
[84] J. Hu, V. Tarasov, A. Agarwal, L. Kimerling, N. Carlie, L. Petit, K. Richardson, *Opt. Express* **2007**, *15*, 2307.
[85] H. Nazeer, H. Bhaskaran, L. A. Woldering, L. Abelmann, *Thin Solid Films* **2015**, *592*, 69.
[86] T. L. Pedersen, J. Kalb, W. Njoroge, D. Wamwangi, M. Wuttig, F. Spaepen, *Appl. Phys. Lett.* **2001**, *79*, 3597.
[87] H. Lin, L. Li, F. Deng, C. Ni, S. Danto, J. D. Musgraves, K. Richardson, J. Hu, *Opt. Lett.* **2013**, *38*, 2779.